Research Article | Vol. 33, No. 6 / 24 Mar 2025 / Optics Express 12603

Optics EXPRESS

Numerical approximation of slowly varying envelope in finite element electromagnetism: a ray-wave method of modeling multi-scale devices

FAN XIAO,[1] JINGWEI WANG,[1] ZHONGFEI XIONG,[1] AND YUNTIAN CHEN[1,2,*]

[1] *School of Optical and Electronic Information, Huazhong University of Science and Technology, Wuhan 430074, China*
[2] *Wuhan National Laboratory of Optoelectronics, Huazhong University of Science and Technology, Wuhan 430074, China*
[*] *yuntian@hust.edu.cn*

Abstract: In this work we propose an efficient and accurate multi-scale optical simulation algorithm by applying a numerical version of slowly varying envelope approximation in finite element method. Specifically, we employ a fast iterative method to quickly compute the phase distribution of the electric field within computational domain and construct a novel multi-scale basis function that combines the conventional polynomial basis function together with numerically resolved phase information of optical waves. Utilizing this multi-scale basis function, finite element methods can significantly reduce the degrees of freedom required for the solution while maintaining computational accuracy, thereby improving computational efficiency. Without loss of generality, we illustrate our approach via simulating the examples of lens groups and gradient-index lenses, accompanied with performance benchmark against the standard finite element method. The results demonstrate that the proposed method achieves consistent results with the standard finite element method but with a computational speed improved by an order of magnitude.

1. Introduction

In the modeling of photonic devices, full-wave modeling techniques, i.e., finite difference time domain (FDTD) [1] or finite element method (FEM) [2], usually solve the vector wave equation with typical computational domains ranging from a few wavelengths to several hundred at most [3], while geometric optics modeling can model large-sized optical devices/systems beyond thousands of wavelengths, as sketched in Fig. 1(a). Either the full-wave modeling or geometric optics modeling via ray tracing (RT) technique [4], focuses on limited length scales of photonic devices, and becomes inadequate to model complex photonic devices/systems, especially those with multi-scale feature sizes. However, the recent trend of photonic devices evolves towards two distinct research directions: 1) photonic devices underpinned by novel mechanisms that contain complex and effective medium; 2) functional devices that continuously demand miniaturization and integration. For instance, metalens [5–7], i.e., seen as an effective yet thin medium, control the flow of light via surfaces and can be flat and thin, thus promise to scale down the size of the optical systems, especially in the context of technology and commercialization development of augmented/virtual reality (AR/VR) [8–11]. Nevertheless, metalens development is challenged by the complexity of the design workflow, which usually consists of simulating millions of subwavelength unit-cells called meta-atoms, in conjunction with millimeter-scale surface hybrid with traditional refractive lens. Another relevant example is light detection and ranging (LiDAR) [12,13], which also integrates photonic integrated circuits with traditional optical components.

#550883 https://doi.org/10.1364/OE.550883
Journal © 2025 Received 5 Dec 2024; revised 9 Feb 2025; accepted 15 Feb 2025; published 11 Mar 2025

Optics EXPRESS

Evidently, both of the two trends have crying needs for multi-scale modeling for navigating the intricacies of photonic engineering that combines advantages of numerical accuracy of full-wave modeling and the large-scale capability of geometric optics modeling.

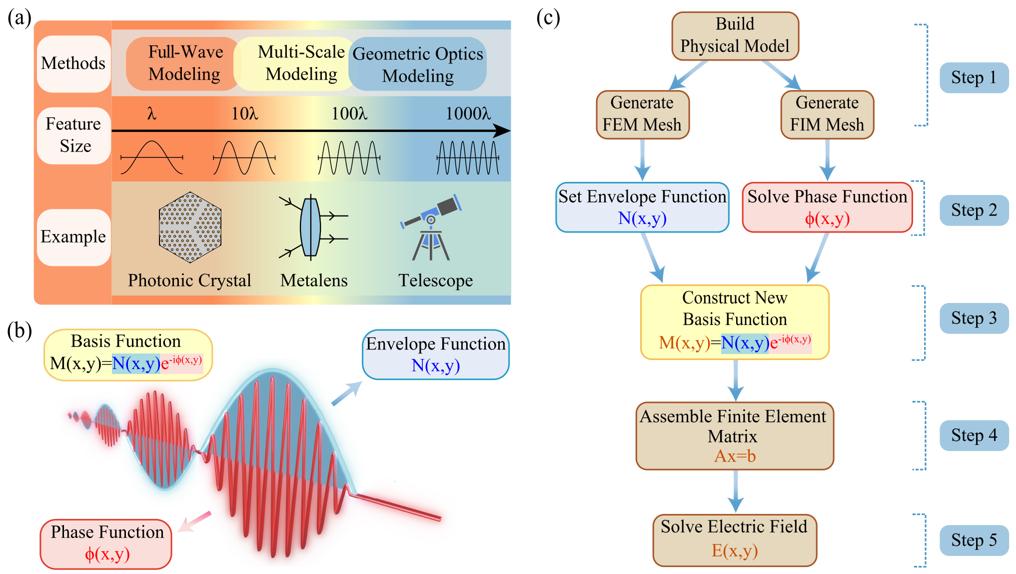

Fig. 1. (a) Length scales, device examples of full-wave/multi-scale/geometric optics modeling, (b) basic idea of RWM for multi-scale devices, (c) workflow of RWM.

In the field of multi-scale FEM method [14], it primarily includes multi-scale basis function techniques, multigrid techniques, and homogenization techniques. Multi-scale basis function techniques [15–17] involve constructing basis functions that can simultaneously capture both macroscopic and microscopic characteristics by utilizing the physical and mathematical properties of the problem to be solved. Multigrid techniques [18–20] enhance computational speed by employing grids of different sizes for problems at various scales. Homogenization techniques [21,22] simplify calculations by approximating the characteristics of microscopic heterogeneous materials using equivalent homogeneous materials. In parallel the current mainstream approach for multi-scale optical systems is to use hybrid methods that combine geometric optics algorithms with full-wave algorithms for simulation. For instance, Leiner et al. integrated RT with FDTD, each simulating different scale regions and exchanging data through predefined files [23–26]. Similarly, companies like Ansys and Synopsys [27] adopt this approach by employing their respective geometric optics software, like Ansys Zemax OpticStudio or CODE V, alongside wave optics software, such as Ansys Lumerical FDTD or RSoft Photonic Device Tools, to simulate devices of different sizes, achieving multi-scale optical system simulation. Additionally, Ziga Lokar et al. employed a combination of rigorous coupled wave analysis (RCWA), RT and transfer matrix method to simulate solar cells [28,29]. Furthermore, Frank Wyrowski et al. combined the Fourier transform with RT to handle the electric field at micro-nano structures [30,31]. Despite the advantages of hybrid methods in addressing multi-scale problems by integrating different algorithms, challenges remain. These include the difficulties of dealing with multiple light sources and ensuring mathematical and physical consistency when exchanging electromagnetic field information between different algorithms.

In this article, we attempt to solve photonic multi-scale problems by encoding the wavefront propagation information solved directly from eikonal equations into the finite element algorithms inherently. Since solving eikonal equations is equivalent to geometric optics modeling via

Optics EXPRESS

RT, thus our proposed approach, coined as the ray-wave method (RWM) onwards, essentially combines advantages from both full-wave and geometric optics modeling. Here, *ray-wave* refers to encoding the wavefront information calculated from optical path of *ray* bundles into *full-wave* modeling algorithms. The ray-wave method can be regarded as a numerical version of slowly varying envelope approximation (SVEA) in FEM [32–34]. In contrast to SVEA-FEM, wherein the phase information is analytically given if the light beam propagates along a main direction, the phase information in RWM is obtained by numerically solving the eikonal equation using fast iterative method (FIM) [35–37], thereby RWM has no restriction on one major directional or bidirectional propagation as assumed in SVEA-FEM. The method proposed in this manuscript can be categorized into multi-scale basis function techniques. It constructs multi-scale basis functions using the physical characteristics of light field transmission, where the phase factor term captures the rapidly varying microscopic elements, and the polynomial term captures the slowly varying macroscopic elements. As such, our RWM is capable of achieving the high numerical accuracy comparable to full-wave modeling and sizable computational domain guaranteed by FIM simultaneously for considerably large and multi-scale photonic devices.

The paper is organized as follows: in Section 2 we present the principles of RWM as well as the processes of the algorithm in detail. In Section 3 we apply RWM to simulate several examples and compare the results with the standard FEM. Finally, Section 4 concludes the paper.

2. Theory and methods

2.1. General Framework

All simulations associated with photonics engineering can be boiled down to solving the following vector wave equation approximated at different levels of simplicity,

$$\nabla \times \boldsymbol{\mu}_r^{-1}(\boldsymbol{r})\nabla \times \boldsymbol{E}(\boldsymbol{r}) - k_0^2\boldsymbol{\epsilon}_r(\boldsymbol{r})\boldsymbol{E}(\boldsymbol{r}) = 0, \tag{1a}$$

$$|\nabla s(r)| - n(r) = 0, \tag{1b}$$

where $\boldsymbol{E}(\boldsymbol{r})$ is the electric field, $\boldsymbol{\epsilon}_r(\boldsymbol{r})$ and $\boldsymbol{\mu}_r(\boldsymbol{r})$ represent the relative permittivity and permeability of the medium, respectively. Here, $k_0 = 2\pi/\lambda_0$, where k_0 and λ_0 represent the wave number and wavelength in free space, respectively. Then, $s(r)$ represents the optical path length from the source and $n(r)$ describes the distribution of the refractive index. Without any approximation, the original vector wave equation given in Eq. (1a) is most difficult to solve. One of the extremely successful approximations is the geometric optics approximation, wherein Eq. (1a) is reduced to the scalar wave equation and is further approximated as the eikonal equation Eq. (1b) under the assumption that field amplitude stays unchanged locally. Notably, the eikonal equation essentially extracts the phase information of propagating waves with incredible accuracy, especially in large-scale scenarios wherein the optical inhomogeneity is weak. Inspired by this simple observation, we decompose the electric field $\boldsymbol{E}(\boldsymbol{r})$ into two components sketched in Fig. 1(b), i.e., $\boldsymbol{E}(\boldsymbol{r}) = \boldsymbol{e}(\boldsymbol{r})e^{-i\phi(\boldsymbol{r})}$, which contains a rapidly varying phase factor $e^{-i\phi(\boldsymbol{r})}$ and a slowly varying envelope term $\boldsymbol{e}(\boldsymbol{r})$. Accordingly, in our RWM, we expand the electric field as $\boldsymbol{E}(\boldsymbol{r}) = \sum_{j=1}^{N} u_j\boldsymbol{M}_j(\boldsymbol{r})$ and adopt a novel multi-scale basis function $\boldsymbol{M}_j(\boldsymbol{r})$ containing a fast oscillation term $e^{-i\phi(\boldsymbol{r})}$ and a slowly varying term $\boldsymbol{e}(\boldsymbol{r})$ as given by

$$\boldsymbol{M}_j(\boldsymbol{r}) = \boldsymbol{N}_j(\boldsymbol{r})e^{-i\phi(\boldsymbol{r})}, \tag{2}$$

where the polynomial function $\boldsymbol{N}_j(\boldsymbol{r})$ denotes the j-th basis function, and $\phi(\boldsymbol{r})$ is the known propagation phase distribution calculated from FIM in geometric optics limitation. When expanding the electric field using the multi-scale basis function, a fundamental assumption is made: it is required that $u_j\boldsymbol{N}_j(\boldsymbol{r})$ can describe the complex amplitude characteristics aside from the rapidly varying phase factor $e^{-i\phi(\boldsymbol{r})}$. $\boldsymbol{N}_j(\boldsymbol{r})$ is a real function, while u_j is theoretically complex.

Optics EXPRESS

So based on merely extending the basis functions, RWM theoretically does not necessarily make any approximation. This work uses the example of two-dimensional TM polarization, where the basis function employs the two-dimensional scalar basis function. As for the generalization of RWM to 3D problem, the wavefronts as well as the 3D vectorial basis function shall be revised accordingly. Notably, according to the variational principle of FEM, the validity of numerical implementation relies on the self-adjointness of the wave-equation operator L under the complex inner product,

$$(\boldsymbol{F}, L\boldsymbol{E}) = (L\boldsymbol{F}, \boldsymbol{E}), \tag{3}$$

where the wave-equation operator $L = \nabla \times \boldsymbol{\mu}_r^{-1}(\boldsymbol{r})\nabla \times -k_0^2\boldsymbol{\epsilon}_r(\boldsymbol{r})$ and F is the test function. See more details in previous works [38–41]. In this regard, the selected complex inner product in the weak form as well as the self-adjointness of L given in Eq. (3) together impose constraints on the material tensor $\boldsymbol{\epsilon}_r(\boldsymbol{r})$ and $\boldsymbol{\mu}_r(\boldsymbol{r})$, i.e., $\boldsymbol{\epsilon}_r^T = \boldsymbol{\epsilon}_r^*$ and $\boldsymbol{\mu}_r^T = \boldsymbol{\mu}_r^*$, implying that the materials are lossless.

The practical implementation of ray-wave modeling consists of three major ingredients: (1) calculating the phase-propagating factor, (2) plugging the phase factor into weak form of FEM for pretreatment of numerical integration and boundary conditions and (3) FEM implementation of weak form, which can be summarized into the following 5 steps illustrated in Fig. 1(c),

(1) Physical models are established for various scenarios, and two meshes with varying sparsity levels are generated for FIM and FEM computations;

(2) Solve the optical path length using FIM on FIM mesh, obtain the phase function from the optical path length, map the phase function on FIM mesh to FEM mesh using interpolation algorithms;

(3) Combine the envelope function with the phase function, construct multi-scale basis functions;

(4) Assemble the finite element matrix based on basis functions and specific boundary conditions;

(5) Solve the finite element matrix to obtain the electric field of the physical model.

To ensure self-consistency, in the next subsection, we will briefly discuss the numerical procedures of calculating propagation phases ϕ in geometric optics approximation using FIM, as well as the technical details of adapting propagating phase numerically into FEM. As a side remark, one notes that both FIM and FEM crucially rely on the mesh, which are actually two independent sets of meshes in RWM. However, we do use the mesh data of FEM to interpolate the propagating phase $\phi(\boldsymbol{r})$ calculated from FIM to preserve the numerical accuracy. Lastly, due to the implementation of parallel solution strategies, the time required for FIM to compute the phase factor can be negligible compared to the solution time of FEM.

2.2. Practical implementation

2.2.1. FIM for solving the propagation phase in geometric optics approximation

We now implement the specific process of applying FIM to compute the phase ϕ based on FIM mesh as outlined in the workflow in Fig. 1(c). This involves employing the Godunov upwind difference scheme [42] to numerically solve the eikonal equation within FIM mesh,

$$\max(D^{-x}u, -D^{+x}u, 0)^2 + \max(D^{-y}u, -D^{+y}u, 0)^2 = n(r)^2, \tag{4}$$

Equation (4) provides the discretized form of the eikonal equation on a two-dimensional Cartesian grid. Here, u is the discrete approximation of phase ϕ at a specific node. The operations

Optics EXPRESS

D^{-p} and D^{+p} denote the forward and backward difference operators, respectively, along the axis $p \in \{x, y\}$. The discretized form on a triangular mesh can be found in the article [36].

FIM aims to solve the eikonal equation to obtain the optical path length at the arrival point of the wavefront, wherein the optical path is converted to optical phase for the construction of multi-scale basis function. One notices that the phase obtained in FIM extends from 0 to positive infinity, preserving the accurate calculation of phase gradient ($\nabla\phi(\boldsymbol{r})$) , since the periodic oscillation of phase within the range of $-\pi$ to π makes it hardly differentiable due to the steep jump of $\phi(\boldsymbol{r})$ from $-\pi$ to π at certain position. In contrast to computing optical path using ray tracing algorithm, we calculate the optical path through the wavefront in FIM, which treats all points on the wavefront as secondary wave sources that emit wave in all directions when updating points [42]. This approach employs the Huygens principle, thus to a certain extent incorporating the diffraction characteristics of light wave, and thereby enables the calculation of phase information of the whole space.

Notably, FIM is unable to handle the scenario where interference occurs, i.e., more than two sets of wave-fronts intersect. Specifically, at points where light rays cross, the solution of the eikonal equation only records the phase of the first arriving wave, thus wavefront information of the rest waves is lost. Inspired by the bidirectional beam envelope method [43], the inclusion of multiple wave-fronts in RWM is possible but beyond the scope of the current paper, which will be studied in our future work.

2.2.2. FEM for solving slowly varying envelope

Provided that the phase distribution $\phi(\boldsymbol{r})$ from FIM is known, we subsequently construct multi-scale basis function $\boldsymbol{M}_j(\boldsymbol{r})$ in conjunction with polynomial basis functions $\boldsymbol{N}_j(\boldsymbol{r})$ as depicted in Fig. 1(c). These multi-scale basis functions are applied to assemble the finite element matrix in FEM to solve electric fields. Following the standard procedure of FEM and choosing the expansion functions as $\boldsymbol{M}_j(\boldsymbol{r})$ and the test functions as $\boldsymbol{M}_i(\boldsymbol{r})^*$, respectively, we can obtain the weak form in practical FEM implementation that corresponds to the vector wave equation in Eq. (1a),

$$\begin{aligned}\int_\Omega \left[\nabla\times\boldsymbol{M}_i(\boldsymbol{r})^*\cdot\boldsymbol{\mu}_r^{-1}(\boldsymbol{r})\nabla\times\sum_{j=1}^{N}u_j\boldsymbol{M}_j(\boldsymbol{r}) - k_0^2\boldsymbol{\epsilon}_r(\boldsymbol{r})\boldsymbol{M}_i(\boldsymbol{r})^*\cdot\sum_{j=1}^{N}u_j\boldsymbol{M}_j(\boldsymbol{r})\right]dV \\ + \int_\Gamma \boldsymbol{M}_i(\boldsymbol{r})^*\cdot\boldsymbol{\mu}_r^{-1}(\boldsymbol{r})\boldsymbol{n}\times\nabla\times\sum_{j=1}^{N}u_j\boldsymbol{M}_j(\boldsymbol{r})dS = 0.\end{aligned} \tag{5}$$

where Γ denotes the boundary that encloses the domain Ω, and $\boldsymbol{n}$ denotes the outward unit normal vector to the boundary of the modeling domain. In Eq. (5), on purpose, we choose the expansion and test functions as a complex conjugate pair to cancel the rapidly varying factor as much as possible, which are given as follows

$$\begin{aligned}\int_\Omega \left[(\nabla\times\boldsymbol{N}_i(\boldsymbol{r})+i\nabla\phi(\boldsymbol{r})\times\boldsymbol{N}_i(\boldsymbol{r}))\cdot\boldsymbol{\mu}_r^{-1}(\boldsymbol{r})\sum_{j=1}^{N}u_j\left(\nabla\times\boldsymbol{N}_j(\boldsymbol{r})-i\nabla\phi(\boldsymbol{r})\times\boldsymbol{N}_j(\boldsymbol{r})\right)\right]dV \\ -\int_\Omega\left(k_0^2\boldsymbol{\epsilon}_r(\boldsymbol{r})\boldsymbol{N}_i(\boldsymbol{r})\cdot\sum_{j=1}^{N}u_j\boldsymbol{N}_j(\boldsymbol{r})\right)dV \\ +\int_\Gamma\left(\boldsymbol{N}_i(\boldsymbol{r})\cdot\boldsymbol{\mu}_r^{-1}(\boldsymbol{r})\boldsymbol{n}\times(\nabla-i\nabla\phi(\boldsymbol{r}))\times\sum_{j=1}^{N}u_j\boldsymbol{N}_j(\boldsymbol{r})\right)dS = 0.\end{aligned} \tag{6}$$

Next, we will illustrate this process through a concrete example, the computation domain of which is Ω surrounded by the closed surface Γ_1 and Γ_2. Without loss of generality, the external plane wave excitation $\boldsymbol{E}^i e^{-ik_0\boldsymbol{k}^i\cdot\boldsymbol{r}}$ enters FEM through boundary condition at Γ_1 boundary, as given

Optics EXPRESS

by

$$\begin{aligned} \boldsymbol{n}\times\nabla\times\boldsymbol{E}(\boldsymbol{r}) - ik_0\boldsymbol{n}\times\boldsymbol{E}(\boldsymbol{r})\times\boldsymbol{n} = \\ \boldsymbol{n}\times(\nabla\times\boldsymbol{E}^i(\boldsymbol{r}))e^{-ik_0\boldsymbol{k}^i\cdot\boldsymbol{r}} - ik_0\boldsymbol{n}\times(\boldsymbol{E}^i(\boldsymbol{r})\times(\boldsymbol{n}-\boldsymbol{k}^i))e^{-ik_0\boldsymbol{k}^i\cdot\boldsymbol{r}}, \end{aligned} \tag{7}$$

where $\boldsymbol{k}^i$ is the incident direction, and $\boldsymbol{n}$ is the unit outward normal vector of the boundary, $\boldsymbol{E}(\boldsymbol{r})$ is the dependent variable that we intend to solve. The scattering light exits through the remaining boundary Γ_2, the boundary condition of which reads,

$$\boldsymbol{n}\times\nabla\times\boldsymbol{E}(\boldsymbol{r}) - ik_0\boldsymbol{n}\times\boldsymbol{E}(\boldsymbol{r})\times\boldsymbol{n} = 0. \tag{8}$$

Substituting Eq. (8) and Eq. (9) into Eq. (6), we derive the linear equation

$$Ax = b. \tag{9}$$

In this formulation, A denotes the stiffness matrix, with the element in the i-th row and j-th column given by:

$$\begin{aligned} A_{ij} = \int_\Omega \left[(\nabla\times\boldsymbol{N}_i(\boldsymbol{r}) + i\nabla\phi(\boldsymbol{r})\times\boldsymbol{N}_i(\boldsymbol{r}))\cdot\boldsymbol{\mu}_r^{-1}(\boldsymbol{r})\left(\nabla\times\boldsymbol{N}_j(\boldsymbol{r}) - i\nabla\phi(\boldsymbol{r})\times\boldsymbol{N}_j(\boldsymbol{r})\right)\right]dV \\ - \int_\Omega \left(k_0^2\boldsymbol{\epsilon}_r(\boldsymbol{r})\boldsymbol{N}_i(\boldsymbol{r})\cdot\boldsymbol{N}_j(\boldsymbol{r})\right)dV + \int_{\Gamma_1+\Gamma_2}\left(\boldsymbol{N}_i(\boldsymbol{r})\cdot ik_0\boldsymbol{n}\times\boldsymbol{N}_j(\boldsymbol{r})\times\boldsymbol{n}\right)dS. \end{aligned} \tag{10}$$

The vector b represents the load vector, with the element in the i-th row given by:

$$\begin{aligned} b_i = \int_{\Gamma_1}\left[\boldsymbol{N}_i(\boldsymbol{r})e^{i\phi(\boldsymbol{r})}\cdot ik_0\boldsymbol{n}\times\left(\boldsymbol{E}^i(\boldsymbol{r})\times(\boldsymbol{n}-\boldsymbol{k}^i)\right)e^{-ik_0\boldsymbol{k}^i\cdot\boldsymbol{r}}\right]dS \\ - \int_{\Gamma_1}\left[\boldsymbol{N}_i(\boldsymbol{r})e^{i\phi(\boldsymbol{r})}\cdot\boldsymbol{n}\times\left(\nabla\times\boldsymbol{E}^i(\boldsymbol{r})\right)e^{-ik_0\boldsymbol{k}^i\cdot\boldsymbol{r}}\right]dS. \end{aligned} \tag{11}$$

Due to the multi-scale nature of computation problems in RWM, the difference in phase velocity between the numerical solution and the exact solution leads to dispersion error, which gradually accumulates as the propagation distance increases. We choose the polynomial basis function $\boldsymbol{N}_j(\boldsymbol{r})$ to be at least quadratic to effectively reduce it. Since $\phi(\boldsymbol{r})$ is a first-order function in most cases, $\nabla\times\boldsymbol{N}_j(\boldsymbol{r})$ and $i\nabla\phi(\boldsymbol{r})\times\boldsymbol{N}_j(\boldsymbol{r})$ are second-order functions, making the integral term a fourth-order function. So, a fourth-order Gaussian integration can achieve full numerical integration accuracy for this polynomial function. By solving Eq. (9), we can determine the electric field distribution within the computational domain. Notably, because the multi-scale basis function $\boldsymbol{M}_j(\boldsymbol{r})$ is complex, the stiffness matrix A is non-symmetric but Hermitian, thus necessitating an appropriate solution method.

2.3. Error analysis

We proceed to discuss the numerical performance of RWM, i.e., the relative error and its dependence as a function of mesh density, which in this context refers to the edge length of the largest triangular element within the mesh. As sketched in Fig. 2(a), we consider a Gaussian beam (beam waist is 2λ, i.e., twice the operating wavelength λ) propagating in a grading refractive index medium, with a distribution given by $n = \sqrt{1 + 0.01[1/\mu m]x[\mu m]}$, as shown by the gradient yellow in Fig. 2(a). The inset of Fig. 2(a) shows the two sets of meshes, i.e., FIM mesh and FEM mesh as colored by solid black lines and solid orange lines respectively, located in the middle of Fig. 2(a) as indicated by the red square. Though FIM mesh is over 10 times coarser than FEM mesh, FIM can still obtain phase values rather accurately by interpolation on FEM mesh points from the values on FIM mesh points.

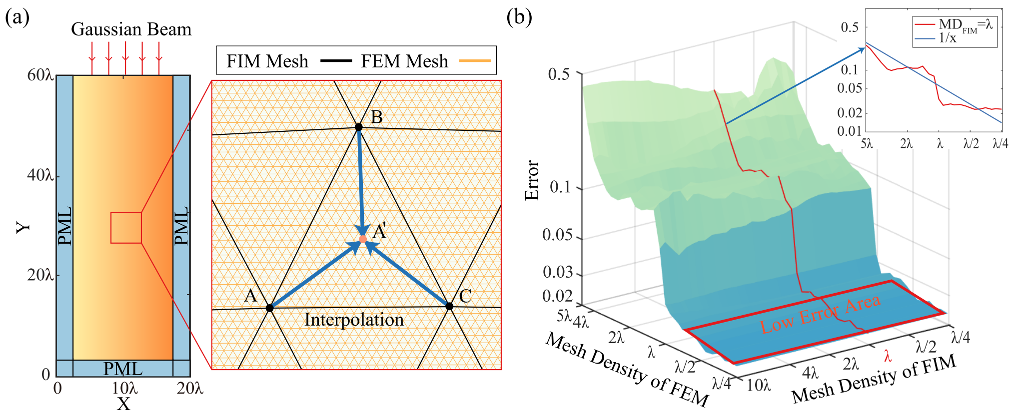

Fig. 2. The results of error analysis for RWM. (a) Model structure. (b) Surface plot of relative error as function of FIM mesh density and FEM mesh density.

Figure 2(b) displays the relative error versus mesh densities, wherein the relative error is defined as follows,

$$\text{error} = \sqrt{\frac{\sum_{i=1}^{N} \|E_i - E_{0i}\|^2}{\sum_{i=1}^{N} \|E_{0i}\|^2}}, \tag{12}$$

where E_{0i} is approximately the ground truth value of the electric field within the i-th triangular element obtained from full-wave FEM commercial software package COMSOL Multiphysics , and E_i is the electric field within the i-th triangular element calculated using RWM, N is the total number of elements in the mesh. Evident from Fig. 2(b), as the mesh density of FIM remains unchanged, the overall error of RWM decreases as the mesh density of FEM increases. While the error of RWM hardly changes against the variation of FIM mesh density for constant value of FEM mesh density. This is because the phase distribution on the sparse FIM mesh can be mapped to a denser FEM mesh via barycentric interpolation for triangles. We focus on the case where FIM mesh density is λ and compare it with the theoretical $1/x$ curve, noting that their convergence is similar. The application of the Godunov upwind difference scheme ensures accuracy in solving the eikonal equation on the sparse FIM mesh, retaining most of the phase information with minimal error.

Due to the intrinsic error of FIM itself at the computation nodes, the numerical error continuously accumulates from the initial point to the surrounding area as the wavefront advances. Nevertheless, as can be observed from Fig. 2(b), within the area marked by the red box, the RWM's errors remain consistently low. In particular, when the mesh densities of both FEM and FIM are λ, the error is only 0.0340. In contrast, when the mesh density is set to $\lambda/5$, the error in FEM results is 0.0264. These data points imply that the aforementioned numerical error from FIM can be neglected. In this regard, we choose FIM mesh density to be 10λ to rapidly obtain phase values, and FEM mesh density to be the value ranging from λ to $\lambda/2$ in practical implementation of RWM. Next, we benchmark the computational time and memory consumption of RWM with previously mentioned consideration of mesh sizes against the results calculated from a commercial software package (COMSOL Multiphysics) through two concrete examples.

3. Two numerical examples

3.1. Projection objective lens

The first example is a key component in optical lithography machines, i.e., the projection objective lens, which usually consists of multiple complex lens systems. Attaining high performance in this aspect is critical for the evolution of lithography technology, directly influencing the precision, speed, and cost efficiency of chip fabrication processes [44,45]. Here, we provide an example to demonstrate the advantages of RWM in simulating projection objective lens. The example is based on a patented system [46], with its size proportionally reduced to fit the simulation range of RWM. Figure 3(a) illustrates the structure, which consists of 14 lenses and has overall dimensions of 80 μm by 300 μm. The incident light is a cylindrical wave with a wavelength of 405 nm, and simulations are conducted for three selected fields of view (FOVs). For the first FOV, the light source is aligned with the optical axis, while for the second and third FOV, light sources are positioned 20 μm and 40 μm away from the optical axis, respectively. In practical cases, anti-reflective coatings are applied to the lens surfaces to reduce stray light from Fresnel reflections. In RWM simulation, it is necessary to add transition boundary conditions [47] on the lens surface, which is suitable for material layers whose thickness is relatively smaller compared to the characteristic size, to simulate the effect of the anti-reflective coating, as Fresnel reflections from the discontinuity in the refractive index can lead to interference fringes. Such fringes disrupt the slow variation of the envelope function, causing an artificial destructive interference with the incident beam. This process effectively eliminates the influence of interference fringes and enhances the simulation accuracy.

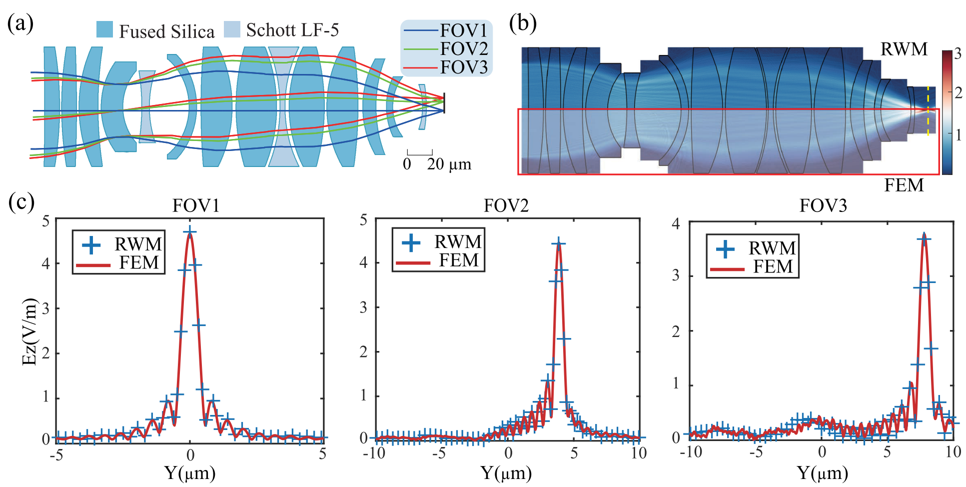

Fig. 3. Simulation results of the projection objective lens.(a) Model structure. (b) Electric fields simulation results of FEM and RWM with FOV1. (c) Comparison of electric fields simulated by RWM and FEM at the image plane under three different FOVs.

Figure 3(b) presents a comparison of the electric field simulation results obtained using RWM and the standard FEM for FOV 1. The upper part of the figure displays the results from RWM, while the lower part (within the red box) shows the results from FEM. Figure 3(c) illustrates the comparison of the electric field intensity between FEM simulation and RWM simulation at the focal plane, specifically along the yellow dashed line in Fig. 3(b), under three FOVs. The primary and secondary maxima of RWM closely align with the standard FEM results across all three FOVs.

Table 1 presents the calculation information and errors of two simulation methods. The error is calculated using the method detailed in Eq. (13). The reference electric fields are obtained from standard FEM simulations with a mesh density of $\lambda/12$. In RWM simulation, FIM mesh density is 10λ and FEM mesh density is $\lambda/1.5$, whereas the standard FEM simulation uses a mesh density of $\lambda/5$. Clearly, compared to the standard FEM, RWM uses only one-tenth of the DOFs, resulting in both the simulation time and the computational resources required for

RWM being only one-tenth of those required for standard FEM, while maintaining a comparable computational error to that of FEM. Because a very sparse mesh is used to solve the phase, the computation time for FIM, added with interpolation time, is less than one second and can thus be considered negligible. Additionally, in the third FOV, the large incident wave angle prevents the transition boundary conditions from eliminating all reflected waves. Consequently, interference occurs on certain surfaces, producing stray light and causing significant errors in RWM. However, this does not affect the accuracy of the focal plane's electric field.

Table 1. Calculation information of RWM and FEM for projection objective lens.

Methods	Degree of Freedom	View	Simulation Time	Computational Resources	Relative Error
FEM	31470915	FOV 1	1403.21s	214.84GB	0.0528
		FOV 2	1404.11s	213.67GB	0.0557
		FOV 3	1405.32s	213.05GB	0.0662
RWM	2800448	FOV 1	54.21s	25.19GB	0.0958
		FOV 2	60.34s	24.40GB	0.1029
		FOV 3	51.90s	23.77GB	0.1361

Furthermore, our local server has a maximum memory capacity of 1548 GB, eliminating the need for external storage during computations. If memory is limited, the computation time for standard FEM will greatly increase, further underscoring the advantages of RWM. In summary, RWM can greatly reduce the DOF required for computation while maintaining high accuracy, representing a significant improvement over standard FEM. Furthermore, it can support various forms and directions of incident waves. However, it may overlook the interference fields generated, potentially affecting accuracy.

3.2. Gradient refractive index lenses

Gradient refractive index (GRIN) lenses, known for their exceptional broadband performance, high directivity, and energy transmission efficiency, are widely employed in various applications [48]. However, the inherently complex refractive index distribution of GRIN lenses introduces significant challenges for conducting precise simulations. Here, we use Mikaelian lens [49], self-focusing fiber and Luneburg lens [50] as three examples to verify the effectiveness of RWM in simulating GRIN lenses. The refractive index distribution of these lenses can generally be expressed as follows:

$$n_1(y) = n_0 \mathrm{sech}(2\pi p y/d) \tag{13a}$$

$$n_2(y) = n_0(1 - Ay^2) \tag{13b}$$

$$n_3(r) = \frac{1}{f}\sqrt{1 + f^2 - (\frac{r}{R})^2} \tag{13c}$$

where n_1, n_2, and n_3 represent the refractive index distribution of Mikaelian lens, self-focusing fiber and Luneburg lens, respectively. d is the thickness of Mikaelian lens, n_0 is the central refractive index along the optical axis, p and A are constants that determine the rate of change of the refractive index. R denotes the radius of the Luneburg lens, and r represents the radial coordinate originating from the center of the lens. The dimensionless parameter f determines whether the focal point is located inside or outside the lens, i.e., the focal point is on the surface of the lens when $f = 1$.

Figures 4(a-c) display the electric field intensity distributions obtained from RWM and standard FEM for three types of lenses. The entire simulation domain measures 50 μm by 70 μm, with a plane wave of 400 nm wavelength incident horizontally. The upper part of the figure presents the simulation results from RWM with FIM mesh density of 2λ and FEM mesh density of $\lambda/1.5$. In contrast, the bottom half in the red box displays the simulation results of standard FEM, utilizing a mesh density of $\lambda/5$. The region delineated by the solid black line represents the area of the lens, while the yellow dashed line indicates the focal plane. Figures 4(d-f) display the comparison of electric fields simulated by RWM and standard FEM at the focal plane. The simulation results of RWM, whether for the main peak or the secondary peak, closely match those of FEM. This demonstrates that RWM is capable of achieving high accuracy simulation of the gradient refractive index system , even when the mesh density is $\lambda/1.5$.

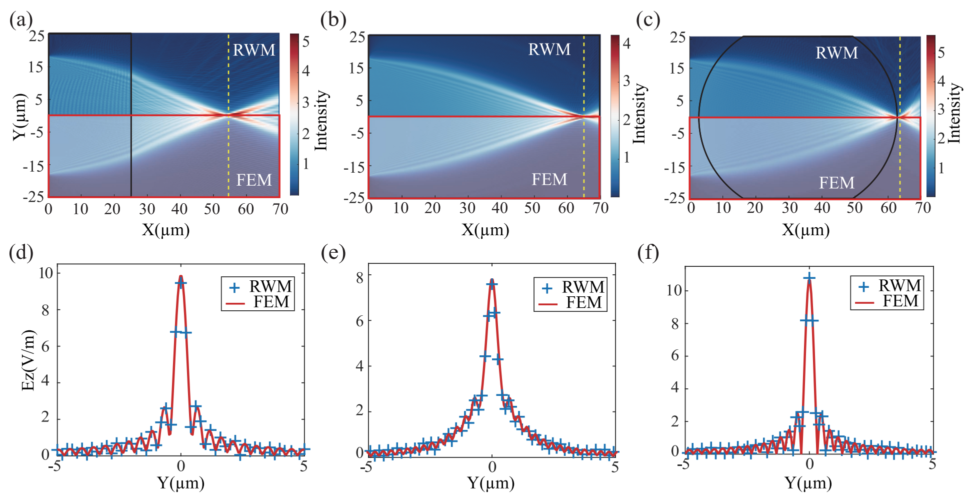

Fig. 4. Simulation results of gradient refractive index lenses. (a-c) Simulation results of Mikaelian lens, self-focusing fiber and Luneburg lens by RWM and FEM, respectively. (d-f) Comparison of electric fields simulated by RWM and FEM at the focal plane of different lenses.

Table 2 presents simulation information. The reference electric fields are conducted from FEM simulation results with a mesh density of $\lambda/15$. Comparing the simulation data between FEM and RWM, it becomes evident that with a reduction in DOFs to one-tenth, the time and computational memory required for RWM are also reduced to merely one-tenth of that needed by the standard FEM. Despite this reduction, the simulation error for RWM remains relatively small.

Table 2. Calculation information of RWM and FEM for gradient refractive index lenses.

Methods	Lens Type	Degree of Freedom	Simulation Time	Relative Error
FEM	Mikaelian Lens	4284775	111.93s	0.0740
	self-focusing fiber	6865537	191.81s	0.0785
	Luneburg Lens	5427785	126.46s	0.0266
RWM	Mikaelian Lens	408797	7.73s	0.1089
	self-focusing fiber	583337	10.78s	0.0970
	Luneburg Lens	512716	10.37s	0.0919

4. Conclusion

In conclusion, we introduce a ray-wave combined numerical algorithm that efficiently and accurately performs simulations of multi-scale optical devices/systems. The phase distribution of electric field within the computational domain is derived by solving the eikonal equation using FIM. A novel multi-scale basis function is then developed by combining polynomial basis functions. Utilizing this multi-scale basis function, FEM can accurately simulate the electric field in optical systems with fewer DOFs, thus enabling the simulation of large multi-scale optical systems. The proposed method performs integrated simulations without separating different devices within the system or involving complex data exchanges between algorithms. Numerical simulations of lens arrays and gradient refractive index lenses validate the accuracy and efficiency of the proposed algorithm. We believe that this method represents a significant advancement in optical system simulation, aiding researchers in more effectively designing and analyzing multi-scale optical devices/systems.

Funding. National Natural Science Foundation of China (No. 61405067); Natural Science Foundation of Hubei Province (No. 2024AFA016); the Innovation Project of Optics Valley Laboratory.

Disclosures. The authors declare that there is a potential conflict of interest regarding the work described in this manuscript. Yuntian Chen, Jingwei Wang and Fan Xiao have filed a patent application related to the method discussed in this paper. The application is currently under review. The details of the patent application are as follows: CN202410681076.9. This patent has not influenced the representation or interpretation of the reported research results.

Data availability. Data underlying the results presented in this paper are not publicly available at this time but may be obtained from the authors upon reasonable request.

References

1. A. Taflove, S. C. Hagness, and M. Piket-May, "Computational electromagnetics: the finite-difference time-domain method," The Electrical Engineering Handbook **3**, 15 (2005).
2. J.-M. Jin, *The finite element method in electromagnetics* (John Wiley & Sons, 2015).
3. C. Kang, C. Park, M. Lee, *et al.*, "Large-scale photonic inverse design: computational challenges and breakthroughs," Nanophotonics **13**(20), 3765–3792 (2024).
4. A. S. Glassner, *An introduction to ray tracing* (Morgan Kaufmann, 1989).
5. M. Pan, Y. Fu, M. Zheng, *et al.*, "Dielectric metalens for miniaturized imaging systems: progress and challenges," Light: Sci. Appl. **11**(1), 195 (2022).
6. Y. Wang, Q. Chen, W. Yang, *et al.*, "High-efficiency broadband achromatic metalens for near-ir biological imaging window," Nat. Commun. **12**(1), 5560 (2021).
7. G. Yoon, K. Kim, D. Huh, *et al.*, "Single-step manufacturing of hierarchical dielectric metalens in the visible," Nat. Commun. **11**(1), 2268 (2020).
8. Y. Ding, Q. Yang, Y. Li, *et al.*, "Waveguide-based augmented reality displays: perspectives and challenges," eLight **3**(1), 24 (2023).
9. J. Xiong, E.-L. Hsiang, Z. He, *et al.*, "Augmented reality and virtual reality displays: emerging technologies and future perspectives," Light: Sci. Appl. **10**(1), 216–230 (2021).
10. J. Zou, T. Zhan, E.-L. Hsiang, *et al.*, "Doubling the optical efficiency of vr systems with a directional backlight and a diffractive deflection film," Opt. Express **29**(13), 20673–20686 (2021).
11. J. P. Rolland and J. Goodsell, "Waveguide-based augmented reality displays: a highlight," Light: Sci. Appl. **13**(1), 22 (2024).
12. N. Li, C. P. Ho, J. Xue, *et al.*, "A progress review on solid-state lidar and nanophotonics-based lidar sensors," Laser Photonics Rev. **16**(11), 2100511 (2022).
13. I. Kim, R. J. Martins, J. Jang, *et al.*, "Nanophotonics for light detection and ranging technology," Nat. Nanotechnol. **16**(5), 508–524 (2021).
14. E. Weinan, *Principles of multiscale modeling* (Cambridge University Press, 2011).
15. H. Kohno, K.-J. Bathe, and J. C. Wright, "A finite element procedure for multiscale wave equations with application to plasma waves," Comput. & Struct. **88**(1-2), 87–94 (2010).
16. Y. Wang, E. Chung, S. Fu, *et al.*, "A comparison of mixed multiscale finite element methods for multiphase transport in highly heterogeneous media," Water Resources Res. **57**(5), e2020WR028877 (2021).
17. E. T. Chung, Y. Efendiev, W. T. Leung, *et al.*, "Multiscale simulations for coupled flow and transport using the generalized multiscale finite element method," Computation **3**(4), 670–686 (2015).
18. L. A. Caudillo-Mata, E. Haber, and C. Schwarzbach, "An oversampling technique for the multiscale finite volume method to simulate electromagnetic responses in the frequency domain," Comput. Geosci. **21**(5-6), 963–980 (2017).
19. Y. Efendiev, J. Galvis, and T. Y. Hou, "Generalized multiscale finite element methods (gmsfem)," J. Comput. Phys. **251**, 116–135 (2013).

20. J. Lu, Y. Chen, D. Li, *et al.*, "An embedded domain decomposition method for electromagnetic modeling and design," IEEE Trans. Antennas Propag. **67**(1), 309–323 (2019).
21. G. Wasselynck, D. Trichet, B. Ramdane, *et al.*, "Interaction between electromagnetic field and cfrp materials: a new multiscale homogenization approach," IEEE Trans. Magn. **46**(8), 3277–3280 (2010).
22. Z. Peng and J.-F. Lee, "Comparisons of heterogeneous multiscale finite element method and localized homogenization process for modeling aperiodic metamaterials," in *Proceedings of the 2012 IEEE International Symposium on Antennas and Propagation*, (IEEE, 2012), pp. 1–2.
23. C. Leiner, S. Schweitzer, V. Schmidt, *et al.*, "Multi-scale simulation of an optical device using a novel approach for combining ray-tracing and fdtd," in *Integrated Optics: Physics and Simulations*, vol. 8781 (SPIE, 2013), pp. 190–198.
24. C. Leiner, W. Nemitz, F. P. Wenzl, *et al.*, "A simulation procedure for light-matter interaction at different length scales," in *Optical Modelling and Design II*, vol. 8429 (SPIE, 2012), pp. 177–184.
25. C. Leiner, S. Schweitzer, F.-P. Wenzl, *et al.*, "A simulation procedure interfacing ray-tracing and finite-difference time-domain methods for a combined simulation of diffractive and refractive optical elements," J. Lightwave Technol. **32**(6), 1054–1062 (2014).
26. C. Leiner, W. Nemitz, S. Schweitzer, *et al.*, "Multiple interfacing between classical ray-tracing and wave-optical simulation approaches: a study on applicability and accuracy," Opt. Express **22**(13), 16048–16060 (2014).
27. Ansys Optics, Synopsys. https://www.ansys.com/ and https://www.synopsys.com/.
28. Z. Lokar, B. Lipovsek, J. Krc, *et al.*, "Performance analysis of rigorous coupled-wave analysis and its integration in a coupled modeling approach for optical simulation of complete heterojunction silicon solar cells," Beilstein J. Nanotechnol. **9**, 2315–2329 (2018).
29. Z. Lokar, B. Lipovsek, A. Razzaq, *et al.*, "Coupled modelling approach for optimization of bifacial silicon heterojunction solar cells with multi-scale interface textures," Opt. Express **27**(20), A1554–A1568 (2019).
30. F. Wyrowski and M. Kuhn, "Introduction to field tracing," J. Mod. Opt. **58**(5-6), 449–466 (2011).
31. M. Kuhn, F. Wyrowski, and C. Hellmann, "Non-sequential optical field tracing," in *Advanced Finite Element Methods and Applications*, (Springer, 2013), pp. 257–273.
32. H. Hoekstra, G. J. Krijnen, and P. Lambeck, "New formulation of the beam propagation method based on the slowly varying envelope approximation," Opt. Commun. **97**(5-6), 301–303 (1993).
33. J. Wang, Z. Wang, L. Liu, *et al.*, "Multi-scale multi-domain hybrid finite element modeling of light propagation," Electromagnetic Sci. **2**(4), 0080232 (2024).
34. K. Morimoto, A. Iguchi, and Y. Tsuji, "Efficient topology optimization of optical waveguide using finite element method based on slowly varying envelope approximation," Optik **226**, 165951 (2021).
35. W.-K. Jeong and R. T. Whitaker, "A fast iterative method for eikonal equations," SIAM J. Sci. Comput. **30**(5), 2512–2534 (2008).
36. Z. Fu, W.-K. Jeong, Y. Pan, *et al.*, "A fast iterative method for solving the eikonal equation on triangulated surfaces," SIAM J. Sci. Comput. **33**(5), 2468–2488 (2011).
37. Z. Fu, R. M. Kirby, and R. T. Whitaker, "A fast iterative method for solving the eikonal equation on tetrahedral domains," SIAM J. Sci. Comput. **35**(5), C473–C494 (2013).
38. Z. Xiong, W. Chen, Z. Wang, *et al.*, "Finite element modeling of electromagnetic properties in photonic bianisotropic structures," Front. Optoelectron. **14**(2), 148–153 (2021).
39. B. Friedman, *Principles and techniques of applied mathematics* (Courier Dover Publications, 1990).
40. W. Chen, Z. Xiong, J. Xu, *et al.*, "Generalized coupled-mode formalism in reciprocal waveguides with gain, loss, anisotropy, or bianisotropy," Phys. Rev. B **99**(19), 195307 (2019).
41. Z. Xiong, W. Chen, P. Wang, *et al.*, "Classification of symmetry properties of waveguide modes in presence of gain/losses, anisotropy/bianisotropy, or continuous/discrete rotational symmetry," Opt. Express **25**(24), 29822–29834 (2017).
42. J. A. Sethian, "Fast marching methods," SIAM Rev. **41**(2), 199–235 (1999).
43. M. A. A. Khushaini and A.-B. M. Ibrahim, "On the optical bistability of ferroelectrics via two-wave mixing: Beyond the slowly varying envelope approximation," Opt. Commun. **381**, 384–390 (2016).
44. W. Ulrich, H.-J. Rostalski, and R. M. Hudyma, "Development of dioptric projection lenses for DUV lithography," in *International Optical Design Conference 2002*, vol. 4832 P. K. Manhart and J. M. Sasian, eds., International Society for Optics and Photonics (SPIE, 2002), pp. 158–169.
45. R. H. Stulen and D. W. Sweeney, "Extreme ultraviolet lithography," IEEE J. Quantum Electron. **35**(5), 694–699 (1999).
46. D. R. Shafer, "Lens usable in the ultraviolet," (1988). US Patent 4,770,477.
47. I. Woyna, E. Gjonaj, and T. Weiland, "Broadband surface impedance boundary conditions for higher order time domain discontinuous galerkin method," COMPEL: The Int. J. for Comput. Math. Electr. Electron. Eng. **33**(4), 1082–1096 (2014).
48. D. T. Moore, "Gradient-index optics: a review," Appl. Opt. **19**(7), 1035–1038 (1980).
49. A. Mikaelian and A. Prokhorov, "V self-focusing media with variable index of refraction," in *Progress in Optics*, vol. 17 (Elsevier, 1980), pp. 279–345.
50. N. Kundtz and D. R. Smith, "Extreme-angle broadband metamaterial lens," Nat. Mater. **9**(2), 129–132 (2010).